True Time Delay Optical Beamforming Network Based on Hybrid Inp-Silicon Nitride Integration

Christos Tsokos [ID], Efstathios Andrianopoulos, Adam Raptakis [ID], Nikolaos K. Lyras, Lefteris Gounaridis [ID], Panos Groumas, Roelof Bernardus Timens [ID], Ilka Visscher [ID], Robert Grootjans, Lennart S. Wefers, Dimitri Geskus, Edwin Klein, Hercules Avramopoulos [ID], René Heideman, Christos Kouloumentas [ID], and Chris G. H. Roeloffzen [ID]

Abstract—We demonstrate a broadband and continuously tunable 1×4 optical beamforming network (OBFN), based on the hybrid integration of indium phosphide (InP) components in the silicon nitride (Si_3N_4) platform. The photonic integrated circuit (PIC) comprises a hybrid InP-Si_3N_4 external cavity laser, a pair of InP phase modulators, a Si_3N_4 optical single-sideband full carrier (SSBFC) filter followed by four tunable optical true time delay lines (OTTDLs), and four InP photodetectors. Each OTTDL consists of eight cascaded thermo-optical micro-ring resonators (MRRs) that impose tunable true time delay on the propagating optical signals. The OBFN-PIC is designed to facilitate the steering of a microwave signal with carrier frequency up to 40 GHz over a continuous set of beam angles. We evaluate the performance of the OBFN-PIC to handle and process microwave signals, measuring the link gain, the noise figure (NF), and the spurious-free dynamic range (SFDR) parameters. Moreover, we assess its beamforming capabilities assuming that the OBFN-PIC is part of a wireless system operating in the downlink direction and feeds a multi-element antenna array. Using microwave signals at 5 and 10 GHz with quadrature amplitude modulation (QAM) formats at 500 Mbaud, we evaluate the performance of the OBFN-PIC under various configurations. We show that error-free performance can be achieved at both operating frequencies and for all the investigated beam angles ranging from 45° to 135°, thus validating its potential for high-quality beamforming performance.

Index Terms—Microwave photonics, optical beamforming network, optical true-time delay lines, photonic integrated circuits.

Christos Tsokos, Efstathios Andrianopoulos, Adam Raptakis, Nikolaos K. Lyras, Lefteris Gounaridis, and Hercules Avramopoulos are with the Photonic Communications Research Laboratory, National Technical University of Athens, Zografou, 15573 Athens, Greece (e-mail: ctso@mail.ntua.gr; efand@mail.ntua.gr; arap@mail.ntua.gr; lyrasnikos@mail.ntua.gr; lgou@mail.ntua.gr; hav@mail.ntua.gr).

Panos Groumas and Christos Kouloumentas are with the Photonic Communications Research Laboratory, National Technical University of Athens, Zografou, 15573 Athens, Greece, and also with Optagon Photonics, Agia Paraskevi, 15341 Athens, Greece (e-mail: pgrou@mail.ntua.gr; christos.kouloumentas@optagon-photonics.eu).

Roelof Bernardus Timens, Ilka Visscher, Robert Grootjans, Lennart S. Wefers, Dimitri Geskus, Edwin Klein, René Heideman, and Chris G. H. Roeloffzen are with the LioniX International BV, AL 7500 Enschede, The Netherlands (e-mail: r.b.timens@lionix-int.com; i.visscher@lionix-int.com; r.grootjans@lionix-int.com; l.wefers@lionix-int.com; d.geskus@lionix-int.com; e.j.klein@lionix-int.com; r.g.heideman@lionix-int.com; c.g.h.roeloffzen@lionix-int.com).

Color versions of one or more figures in this article are available at https://doi.org/10.1109/JLT.2021.3089881.

Digital Object Identifier 10.1109/JLT.2021.3089881

I. INTRODUCTION

Beamforming is a well-known technique in modern radar and wireless communications systems for forming and steering single or multiple highly directional beams into specific directions [1]. Using a multi-element antenna array, beamforming networks apply excitation signals to each antenna element (AE) with relative time delays that correspond to the intended beam angles. Especially, in systems operating in the millimeter-wave and sub-terahertz regime, beamforming is of great importance, as it can compensate for the severe free-space path loss and can increase the signal-to-noise-plus-interference ratio (SNIR) improving the overall system performance [2].

Microwave photonics have been in the research spotlight thanks to their ability to offer equal or even superior performance compared to the electrical beamforming networks and support ultra-wideband operation, with lower power consumption and immunity to electromagnetic interference [3]–[4]. Initial efforts involve mainly implementations of true time delay (TTD) optical beamforming networks (OBFNs) based on fiber segments of various length [5]–[6], multi-core [7]–[8] and highly dispersive fibers [9]–[10], fiber Bragg gratings [11]–[12], spatial light modulators [13]–[14], micro-optics [15]–[17], and semiconductor optical amplifiers [18]–[19]. In addition, implementations that approximate the TTD operation using optical phase shifters have also been proposed [20]–[21]. Although important for validation of the system concept, these demonstrations are based mainly on bulky fiber-optics components which have the disadvantages of large size, high cost, and lead to low system stability.

Leveraging the advancements of the photonic integration technology, various integrated OBFNs based on optical true time delay lines (OTTDLs) have been reported. Representative works include OTTDLs based on highly dispersive photonic structures such as photonic crystal waveguides and subwavelength grating waveguides [22]–[24]. In these approaches, the group index and the dispersion coefficient of the waveguides are controlled by the design characteristics of these structures, which, however, impose strict requirements on the lithography process. Alternative approaches are based on switchable waveguide delay lines (SWDLs), which control the introduced time delay in each optical path by switching between waveguides with various lengths [25]–[29]. Despite their simplicity in terms of configuration, these schemes feature by default limitations in their scaling, when a large set of steering angles is required. Within the context of satellite communication networks, a modular

photonic-aided payload receiver based on four Mach-Zehnder delay interferometers has also been reported [30]. However, for its system demonstration, a high number of optical amplifiers and fiber-optic components were required, thus increasing the system complexity. Finally, OTTDLs utilizing optical all-pass filters in the form of micro ring-resonators (MRRs) have been extensively investigated and reported, thanks to their small footprint and ability to select in a continuous way the intended beam angle [31]–[34]. Due to the constant delay-bandwidth product of the MRR, multiple cascaded MRRs are required to achieve broadband operation. In most of the aforementioned works, the photonic integrated circuits (PICs) comprise only the OTTDL network, and in only two demonstrations, they also comprise optical modulators and photodetectors but not laser sources [26], [30].

The technological leap that enabled the demonstration for the first time of a fully functional OBFN in integrated form was the combination of two powerful and complementary photonic integration platforms, i.e., the ultra-low loss (0.1 dB/cm) proprietary Si_3N_4 platform of LioniX Int., known as TriPleX, and the InP platform of Fraunhofer Heinrich Hertz Institute [35]. Their hybrid combination brings the best-of-breed of both platforms and leads to fully functional PICs without need of utilizing external optical components (neither active nor passive ones). Two types of such fully integrated OBFNs have been reported so far [36]–[37]. The first one involves an SWDL-based OBFN with 3-bit resolution [36], while the second one a 1×4 OBFN based on four parallel OTTDLs with 8 cascaded MRRs each [37]. Although key RF measurements were reported in both works, no system experiments were made to give an insight into the expected beamforming performance.

In this work, we demonstrate a fully integrated 1×4 TTD-OBFN based on the InP and TriPleX platforms that can support the generation and steering of a single microwave beam over a continuous set of angles, and we provide for the first time to our knowledge a concrete evaluation of its system performance. The integrated InP components include a pair of high-speed phase modulators and a quad array of photodetectors, whereas the TriPleX platform hosts a single-sideband full carrier optical (SSBFC) filter and four OTTDLs with thermally tunable MRRs. Moreover, a high-power external cavity laser is also part of the PIC consisting of an InP gain section and an external cavity in the TriPleX part of the circuit. Fig. 1 illustrates the packaged OBFN-PIC. It is of 16 mm × 19 mm size, and includes 21 fiber pigtails, 6 RF connectors, and four connectors for flat electrical cables to control the 79 heating electrodes of the circuit. The experimental evaluation of the OBFN-PIC is performed in two stages. In the first one, we measure the link gain, the noise figure (NF), and the spurious-free dynamic range (SFDR) of the microwave photonics link. In the second stage, we assess the beamforming performance of the circuit, considering that the OBFN-PIC is part of a wireless system operating in the downlink direction and feeds a multi-element antenna array. Using modulated microwave signals with 5 and 10 GHz carrier frequencies, quadrature amplitude modulation (QAM) formats, and 500 Mbaud symbol rate, we evaluate the performance of the OBFN-PIC under various beamforming configurations via the
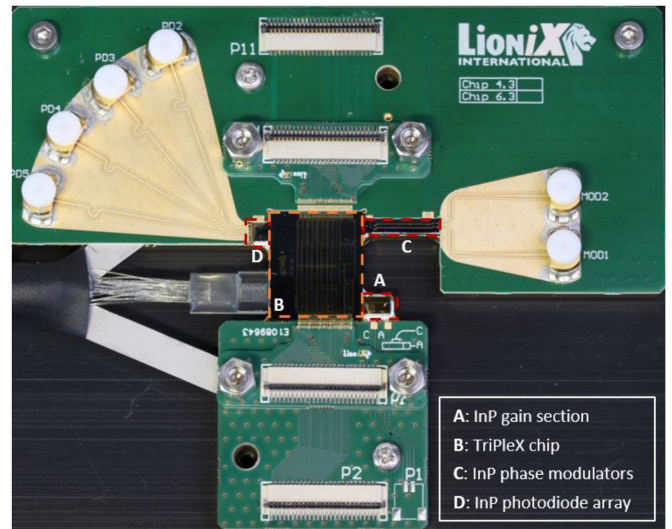

Fig. 1.   Picture of the 1×4 fully integrated OBFN-PIC comprising three InP chips (red dashed lines) that host the laser's gain section, the phase modulators, and the photodiode array, as well as a TriPleX chip (orange dashed lines) that hosts the cavity of the laser, the SSBFC filter, the 1×4 splitter, and the 1×4 OBFN.

analysis of the expected radiation patterns and the calculation of both the error-vector magnitudes (EVMs) and bit-error ratios (BERs) of the decoded signals at the intended beam angles.

The remainder of the manuscript is organized as follows: In Section II, we describe in detail the key components and units of our fully integrated OBFN-PIC. In Section III we present the experimental setup for the system evaluation of the OBFN-PIC and the corresponding experimental results. Finally, in Section IV we provide an outlook, and we conclude.

II. OBFN-PIC ARCHITECTURE

The schematic of the 1×4 OBFN-PIC is presented in Fig. 2. It consists of a waveguide-based external cavity laser, a pair of phase modulators, an optical SSBFC filter followed by four continuously tunable OTTDLs, and an array of four photodiodes. All the individual PICs have been fabricated with angled facets (7°) to minimize the return loss due to light back reflection. Additionally, adiabatic mode converters with a length of 1 mm are integrated on the TriPleX at the interfaces with the InP chips to achieve a mode profile matching between the platforms and minimize the coupling loss. In the paragraphs below, we describe the operation and the design characteristics of the individual units and their main components.

A. Waveguide-Based External Cavity Laser

The hybrid integrated laser uses an InP semiconductor optical amplifier as gain section (GS) and a TriPleX waveguide feedback circuit that extends the cavity length. The extension is enabled by two MRRs that are placed inside a loop mirror in Vernier configuration. The circumferences of the two MRRs are 787 and 813 μm, respectively. A tunable coupler, implemented as a balanced Mach-Zehnder interferometer (MZI) is employed to
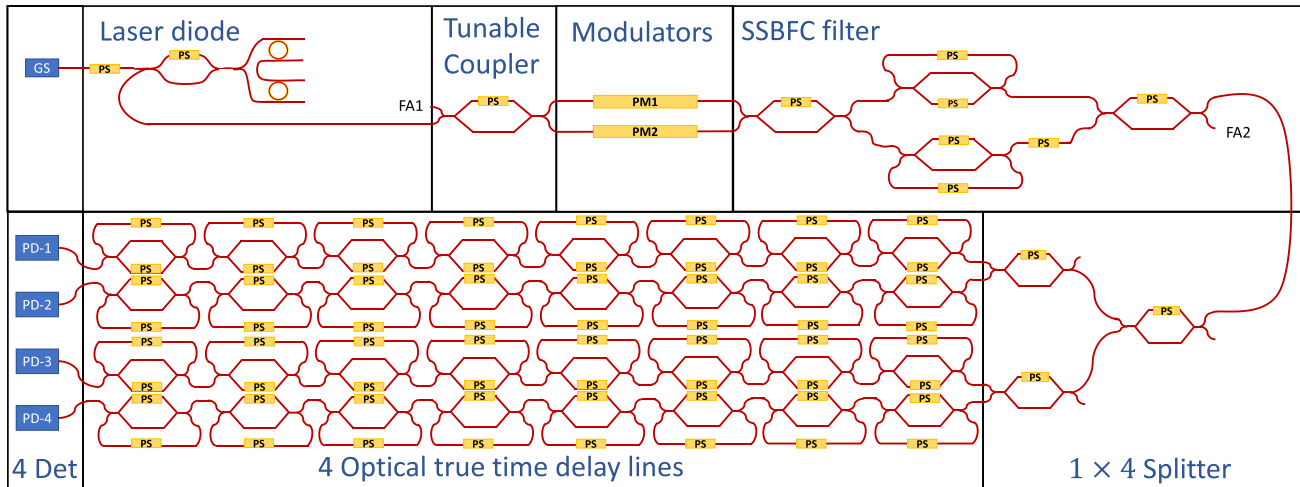
Fig. 2. Schematic view of the fully hybrid integrated 1×4 OBFN-PIC. It comprises a hybrid InP-TriPleX external cavity laser, two InP phase modulators, a TriPleX SSBFC filter followed by a 1×4 splitter, and four OTTDLs based on 8 MRRs each, and four InP photodetectors. .

couple the light out of the laser cavity, while the phase of the light is tuned by an additional phase shifter prior to the MZI. The laser is fully tunable across the C-band (1530-1565 nm) and can exhibit linewidths below 1 kHz [38]. The typical output power of the laser measured at the fiber array port after the optical filter (FA 2 in Fig. 2) is 10 mW.

B. Optical Phase Modulator

In the modulation unit, the microwave signal that will be processed by the OBFN is frequency up-converted and brought to the optical domain via the phase modulation of the optical carrier generated by the external cavity laser. In our PIC, two InP phase modulators with 35 GHz 3-dB analog bandwidth have been integrated for redundancy purposes although only one is required. During the experimental testing process, PM1 was selected due to its superior RF performance. The InP chip is butt-coupled to the TriPleX platform and the average coupling loss is 4.9 dB per facet. An important parameter of the phase modulator is the half-wave voltage V_π, which dictates the voltage that should be applied to achieve a π-phase shift. In microwave photonics systems, optical phase modulators with low V_π are of great importance because the power of the fundamental tone can be maximized after the photodetection stage with lower RF input power [39]. Fig. 3 presents the measured V_π of PM1 as a function of the modulation frequency. The measurement was based on the optical spectrum analysis method which calculates the V_π at a specific modulation frequency by measuring the intensity ratio between the first sidebands and the optical carrier, for a given driving signal with known frequency and amplitude [40]. As observed, the V_π is below 3 V for frequencies up to 10 GHz and increases to 8.1 V at 35 GHz.

C. Optical SSBFC Filter and OTTDL Units

The key optical component of both the SSBFC filter and the OTTDLs is the tunable MRR implemented as a balanced MZI, where one output port is fed back to the input port, forming
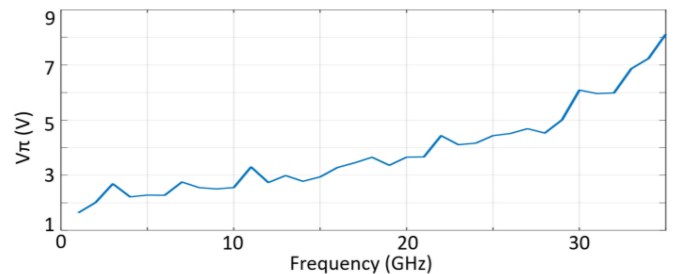

Fig. 3. Measured half-wave voltage, V_π (V), of the phase modulator as a function of the modulation microwave frequency.
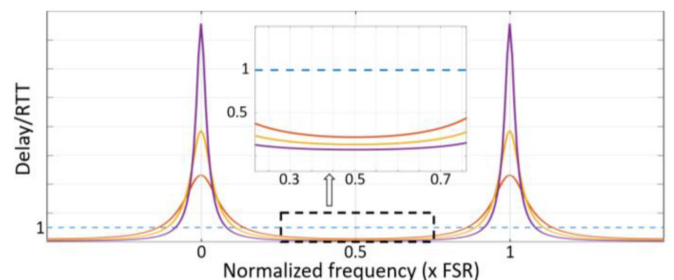

Fig. 4. Imposed delay by an MRR for different values of the coupling coefficient (k) of the companion MZI.

a feedback loop mechanism. The operation of the MRR is controlled by two thermal phase shifters, which reside in one of the arms of the MZI and in the feedback loop waveguide, respectively. The phase shifter in the MZI arm controls the coupling coefficient (k) of the MRR, and thus the power of the optical signal coupled to the feedback loop waveguide, whereas the second phase shifter controls its optical phase (φ) [41], [42].

Therefore, the continuous tuning of both phase shifters provides direct control on the quality (Q)-factor of the MRR and on the true time delay imposed by the MRR on the optical signal [41],[42]. Fig. 4 depicts the delay normalized to the round-trip
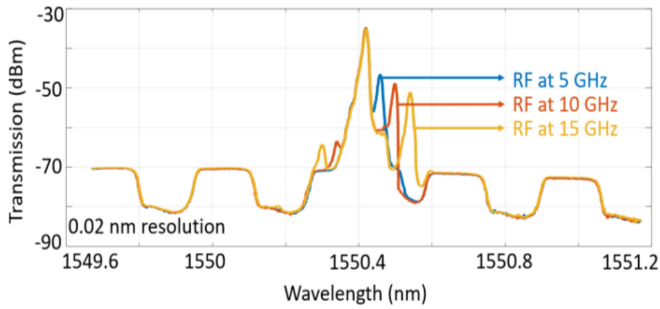
Fig. 5. Experimental optical spectra at the output of the SSBFC filter when driving the PM1 with a 5 GHz, 10 GHz, and 15 GHz sine waves.

time (RTT) imposed by a single MRR over one free spectral range (FSR) as a function of the coefficient k. In the case of k equal to 1 (blue-dashed line), the delay is unitary and the MRR operates as a simple time delay line without spectral selectivity. In the other cases, the k falls within the range $k_c \leq k \leq 1$, where k_c represents the value of k in the case of critical coupling. As observed, delays that are multiple to the RTT can be imposed at the resonance frequencies, whereas delays equal to a fraction of the RTT can be introduced at frequencies off-resonance.

Assuming operation with microwave signals with peak-to-peak voltages lower than V_π, the phase modulated optical signal comprises the optical carrier and two sidebands with opposite phase, and with frequency offset dictated by the frequency of the microwave carrier. If this optical signal is incident on a photodiode, the microwave signal cannot pass on the generated photocurrent due to the square-law of the photodetection process and gets lost. To prevent this loss, an SSBFC filter is deployed to suppress one of the two sidebands [43]. The filter comprises an asymmetric MZI having both its arms coupled to an MRR. The round-trip length of the MRRs should be twice as large as the inter-arm path length difference of the asymmetric MZI in order to maximize the extinction ratio (ER) between the passbands and stopbands [43]. Taking into account that the OBFN is aimed to operate up to 40 GHz, the FSR of the MRRs is set to 20 GHz and the FSR of the asymmetric MZI to 40 GHz. Fig. 5 depicts the optical spectra at the output of the optical SSBFC filter when driving the PM1 with 5, 10 and 15 GHz sinusoidal signals. The left sidebands of the optical carrier are suppressed with respect to the right ones by 12 dB, which corresponds to the ER of the filter, while the FSR of the filter is 40 GHz. It should be noted that the power transfer function of the SSBFC filter is plotted with a half FSR wavelength shift relative to the spectra of the filtered optical signals. This is due to the fact that the broadband noise source used for the extraction of the optical spectra was coupled to the upper port of the tunable coupler prior to the modulator (FA 1 in Fig. 2), whereas the unmodulated optical carrier was coupled to the lower port.

The output signal of the SSBFC filter is fed to the four OTTDLs via a 1×4 splitter based on a combination of three MZIs. The power of the signals at the output of the splitter can be controlled by proper adjustment of the coupling coefficients of the MZIs. Therefore, any difference in the optical propagation losses between the subsequent OTTDLs can be compensated.

More importantly, various amplitude tapering schemes can be used for enhanced beam shaping [1]. Each OTTDL comprises 8 cascaded MRRs with 22 GHz FSR that can be tuned independently. The round-trip length of the MRRs is 0.8 cm which results to a round-trip loss equal to 0.08 dB. The total true time delay at the output of each OTTDL is the sum of the delay imposed by each MRR. In order to steer a microwave beam to an intended angle (θ), the total time delay imposed by each OTTDL should be set as follows [1]:

$$t_n = \frac{[(n-1) \cdot d \cdot \cos(\theta)]}{c} \quad 1 \leq n \leq 4 \tag{1}$$

where d the distance between adjacent AEs, c the speed of light in air, and n the number of the OTTDLs. The thermal crosstalk between the MRRs remains as low as -17 dB by maintaining a distance of 250 μm between the heating electrodes and the adjacent optical waveguides.

D. Photodetectors

An InP quad photodetector array is used for the conversion of the microwave signals from the optical back to the RF domain. The analog bandwidth of the photodiodes is more than 40 GHz, while their responsivity is 0.8 A/W. The generated photocurrents are proportional to the incident light powers and are converted to equivalent voltage signals using 50-ohm resistance loads. The average coupling loss between the TriPleX platform and InP detector chip is 2 dB per facet. When the MRRs of the OTTDLs impose zero additional delay, the total waveguide propagation loss from the output of the external cavity to each photodiode is 1.75 dB. A waveguide break at the optical path of the bottom photodiode (PD 4), adds significant losses that render this photodiode unable to detect the optical signal from the corresponding OTTDL. Therefore, in our experimental testing, only the top three PDs and OTTDLs were utilized.

III. EXPERIMENTAL PERFORMANCE EVALUATION

A. Link Gain, Noise Figure and Spurious Free Dynamic Range

The link gain reveals the gain (or loss) imposed by a microwave photonics system on the power of the input microwave signal as a function of its frequency. Therefore, the link gain from the input of the PM1 at the output of each PD can be expressed as the magnitude of the forward transmission parameter S21. The measurement of the S21 coefficient was performed using a 2-port calibrated Vector Network Analyzer (VNA) with 40 GHz 3-dB analog bandwidth. The output port of the VNA was connected to the PM1 and generated sinewaves with frequencies varying from 0.04 GHz to 40 GHz while the input port was connected successively to the three PDs. During these measurements, the central wavelength of the unmodulated optical carrier was located at the edge of the passband of the SSBFC filter, while all the companion MZIs of the MRRs of the OTTDLs were set at k equal to 1. Fig. 6 shows the link gain for the microwave photonics links PM1-PD1, PM1-PD2 and PM1-PD3, taking also into account the propagation loss induced by the printed circuit boards. The maximum link gain of the PM1-PD1 link is -36.98 dB at 2.6 GHz, of the PM1-PD2 link is -37.23 dB at
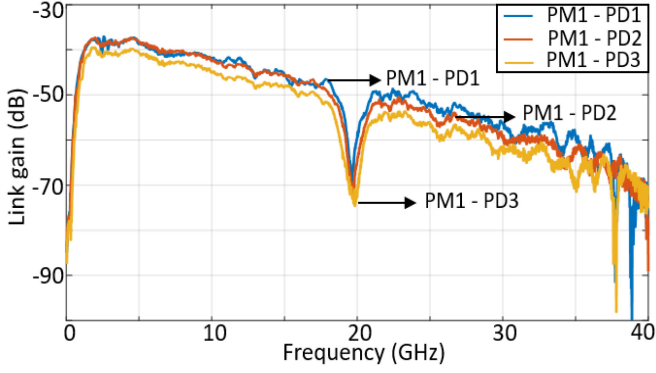
Fig. 6 Link gain measurements for the microwave photonic links,PM1-PD1, PM1-PD2, and PM1-PD3. All the ring resonators of the OBFN are set to off-resonance state.
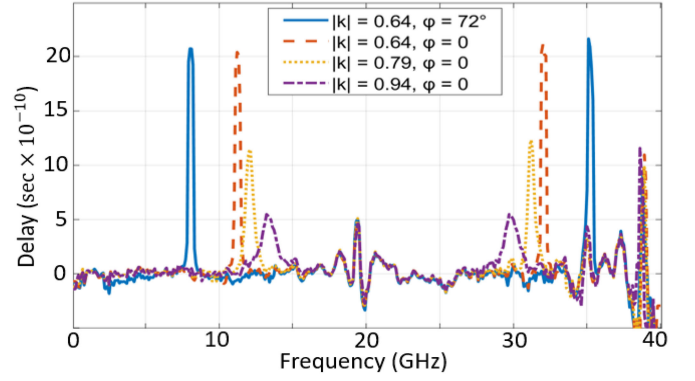

Fig. 7. Imposed delay by one MRR for different coupling coefficients of the MZI and phase shifts on the feedback loop waveguide.

4.6 GHz and of the PM1-PD3 link is -39.39 at 2 GHz. As observed, while increasing the operating frequency, the link gain decreases mainly due to the frequency response of the phase modulator and the PDs, and the increase of the V_π. For microwave frequencies below 1 GHz, between 18 and 21 GHz, and above 39 GHz, the SSBFC filter allows both sidebands of the modulated optical signal to pass through, imposing significant losses. In addition to the link gain, two essential RF parameters that reveal the performance of any microwave photonics system are the NF and the SFDR. The NF describes the degradation of the signal-to-noise ratio (SNR), caused by the microwave photonics system, and can be expressed as follows [39]:

$$\text{NF [dB]} = P_N - G - k_B \cdot T \tag{2}$$

where P_N the noise power spectral density, G the link gain, k_B the Boltzmann's constant and T the operating temperature. Using a 50 GHz electrical spectrum analyzer and terminating the input of the PM1 with a 50-ohm load terminator, we found the noise power density at the outputs of the photodiodes equal to -171.75 dB/Hz, which corresponds to the minimum detectable power density by our equipment. Therefore, the NF can be calculated at different frequencies, replacing the value of the link gain from Fig. 6, and considering the temperature equal to 30°C. Indicatively, the NF of the PM1-PD1 link at 5 and 10 GHz is equal to 42.19 dB and 47.48 dB, respectively. Without the limitation imposed by the equipment, the actual value of the NF could be even lower. Taking into account that the amplitude of the photocurrents was below 0.3 mA, it can be assumed that our system is limited only by the thermal noise, and thus the impact of the other noise sources is negligible [39]. In this case, P_N is equal to the thermal noise and the NF at 5 GHz and 10 GHz is 38.28 dB and 41.95 dB, respectively.

The nth-order SFDR defines the range of input powers over which the output fundamental tone is above the noise floor whilst all nth-order intermodulation distortion tones are less than or equal to the noise floor and is expressed as follows [39]:

$$\text{SFDR}_n \left[\text{dB} \cdot \text{Hz}^{(n-1)/n} \right] = \frac{n-1}{n} \{ \text{OIP}_n - P_N \} \tag{3}$$

where OIP_n the output power at the intersection of the response of the fundamental and the nth-order distortion tones. The OIP_n

can be calculated measuring the power of the fundamental and distortion tones at the same input power [39]. To do that, a standard two-tone experiment was carried out at the PM1-PD1 link. The pair of tones was centered around 5 or 10 GHz with a 200 MHz frequency interval in either case. The OIP_2 and OIP_3 around 5 GHz are -32.8 dBm and -38.8 dBm, respectively and around 10 GHz are -38.3 dBm and -40.6 dBm, respectively. Assuming a noise floor equal to the thermal noise at 30°C, the SFDR_2 and SFDR_3 around 5 GHz are 70.5 dB·$\text{Hz}^{1/2}$ and 89.9 dB·$\text{Hz}^{2/3}$, respectively whereas around 10 GHz are equal to 67.7 dB·$\text{Hz}^{1/2}$ and 88.8 dB·$\text{Hz}^{2/3}$, respectively.

B. Delay Measurements and System Evaluation

The delay imposed by each OTTDL was measured using the VNA which calculates the delay from the derivative of the phase of the forward transmission coefficient, S21, with respect to the frequency. Fig. 7 shows the imposed delay by a single MRR of the OTTDL that corresponds to PD1 for different cross-coupling coefficients of the companion MZI, and for different phase shifts applied in the feedback loop waveguide. Each delay peak corresponds to a resonance frequency of the MRR, that falls within the passbands of the optical filter. Its microwave frequency is determined by the frequency offset between the MRR's resonance and the optical carrier. Due to the difference between the FSRs of the optical filter (i.e., 40 GHz) and the MRRs (i.e., 22 GHz), each MRR can impose either one or two delay peaks simultaneously, within our bandwidth of interest. Assuming that the optical carrier is placed at the edge of the passband of the optical filter, each MRR imposes two delay peaks if the minimum frequency offset between the resonance frequencies that falls within the passbands of the filter and the optical carrier, $|f_{\text{off}}|_{\text{min}}$, is within the frequency ranges from 0 GHz to 2 GHz and from 4 GHz to 20 GHz. Within this case, the frequency difference between the two delay peaks can be expressed as follows:

$$\Delta f \text{ [GHz]} = \begin{cases} \text{FSR}_{\text{MRR}} - 2 \cdot |f_{\text{off}}|_{\text{min}}, \\ \quad 0 \, GHz \leq |f_{\text{off}}|_{\text{min}} < 2 \, GHz \\ 2 \cdot (\text{FSR}_{\text{MRR}} - |f_{\text{off}}|_{\text{min}}), \\ \quad 4 \, GHz \leq |f_{\text{off}}|_{\text{min}} < 20 \, GHz \end{cases} \tag{4}$$
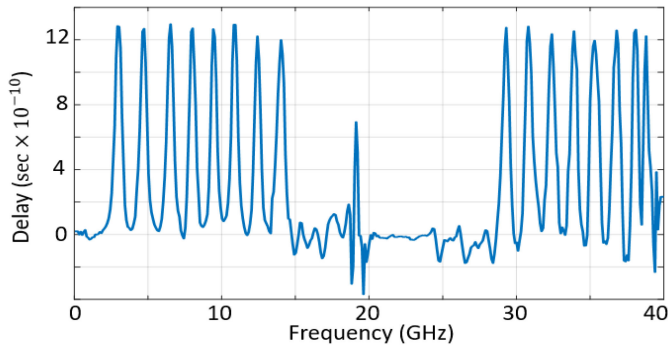
Fig. 8.   Imposed delay by the OTTDL that corresponds to PD1, setting all the MRRs at adjacent resonance frequencies.
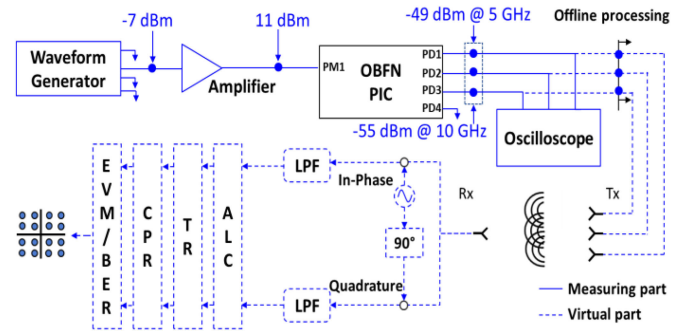

Fig. 9.   Experimental setup for the system evaluation of the OBFN-PIC using QAM modulated signals at 5 GHz and 10 GHz. It consists of a measuring part (blue solid lines) and a virtual part (blue dashed lines).

In all the other cases, the MRR imposes a single delay peak. For an example, the blue curve in Fig. 7 has a delay peak around 8.5 GHz, which means that also the $|f_{off}|_{min}$ is 8.5 GHz, and that the same MRR induces a second delay peak around 35.5 GHz. Fig. 8 presents on the other hand the time delay that is imposed by the same OTTDL, when all of the eight MRRs are tuned.at adjacent resonance frequencies. The additional delay peaks observed at around 19 GHz and 39 GHz in both figures are imposed by the optical SSBFC filter. More specifically, the optical filter imposes almost a flat delay over the passband but at the transition bands, it imposes a delay peak [43]. Both the cross-coupling coefficient and the phase shifter of the feedback loop waveguide of each MRR are controlled by control electronic circuits that provide 0.001 V driving resolution from 0 to 18.75 V, which corresponds to a 2π phase shift. Taking into account that the phase shift is proportional to the square of the applied voltage, the minimum delay shift that can in principle be achieved by a single MRR at either on-resonance or off-resonance frequencies is well below the pico-second regime. The maximum delay that can be imposed by an OTTDL is 1900 ps over a bandwidth of 600 MHz with delay ripple equal to 1 ps. For this specific bandwidth and delay ripple, the delay resolution was measured equal to 1 ps.

The beamforming capabilities of the OBFN-PIC are demonstrated by emulating a wireless system that operates in the downlink direction. In this system, the output microwave signals of the OBFN-PIC are emitted by a 3-element antenna array that forms a single beam directed to a single user. Fig. 9 presents the experimental setup for the performance evaluation of the OBFN-PIC utilizing high-order QAM microwave signals. It consists of a measuring part that includes the actual experimental testbed and a virtual part that includes the offline processing steps. More specifically, in the measuring setup a 65 GSa/s arbitrary waveform generator produces either quadrature phase-shift keying (QPSK) or 16-QAM microwave signals at 5 or 10 GHz carrier frequency. The symbol rate of the microwave signals is set at 500 Mbaud, while their spectral content is confined around their microwave carrier using a raised-cosine pulse shaping filter with roll-off factor equal to 1. The microwave signals are amplified up to 11 dBm by a broadband and low-noise amplifier to drive the PM1. In the OBFN-PIC, the external cavity laser emits a continuous wave signal with central wavelength at 1550.42 nm,

which is fed via the tunable coupler to the PM1. The modulated optical signal is subsequently processed by the SSBFC filter, which is configured to have flat passbands and stopbands with ER and FSR equal to 12 dB and 40 GHz, respectively. At the output of the filter, the signal is equally split into three copies that are coupled to the upper three OTTDLs of the OBFN. The signals at the output of the OBFN are detected by the PD array and are sampled by a 4-channel real-time oscilloscope with 70 GHz analog bandwidth and 256 GSa/s sampling rate, within a 200 μsec time window. As a result of this sampling process, three vectors containing 51.200.000 samples each, are acquired and stored in the internal memory of the oscilloscope.

Within the virtual part, the stored samples are further processed offline for the calculation of the radiated field assuming that the detected signals are transmitted by a linear 3-element antenna array with omnidirectional AEs. The spacing between successive AEs is set at $\lambda/2$. For each experimental case, it is also assumed that a single omnidirectional antenna is placed at a specific nominal beam angle and acts as the receiving antenna to detect the radiated field. The calculated microwave field is down-converted to the baseband using a local oscillator at the carrier frequency and is analyzed back into its in-phase and quadrature components. Finally, a sharp low-pass filter (LPF) with 500 MHz 3-dB bandwidth is applied to each component to filter out the unwanted spectral content at higher frequencies.

A standard set of digital signal processing (DSP) algorithms is utilized to properly decode and evaluate the quality of the received baseband signal. First, an amplitude level correction (ALC) algorithm normalizes the power of the signal to a specific power level dictated by the modulation format. Next, a time recovery (TR) algorithm estimates and removes the timing error offset that is inevitably generated, since the waveform generator and the oscilloscope are not synchronized. Subsequently, the carrier phase recovery (CRP) algorithm removes the phase noise that it is introduced by the waveform generator and the oscilloscope. Finally, the acquired samples are used for the construction of the constellation diagrams and the calculation of the EVM and the BER in order to evaluate the beamforming performance and the overall quality of the transmission system. Table I summarizes the three cases that have been experimentally investigated, presenting for each one of them the corresponding

TABLE I
MODULATION AND BEAMFORMING PARAMETERS OF THE EVALUATION CASES

	Format	Symbol rate (Mbaud)	RF carrier (GHz)	Pulse shaping	Roll-off factor	Beam angles (°)
Case 1	QPSK	500	5	Raised Cosine	1	45, 60, 70, 90, 110, 120, 135
Case 2	16-QAM	500	5	Raised Cosine	1	
Case 3	QPSK	500	10	Raised Cosine	1	

Fig. 11. (a) Array factor of the 500 Mbaud QPSK signal modulated with a 10 GHz microwave carrier and steered at 60°. (b)-(d) Constellation diagrams of the received signal at the observation angle 60°, 20° and 110°, respectively.
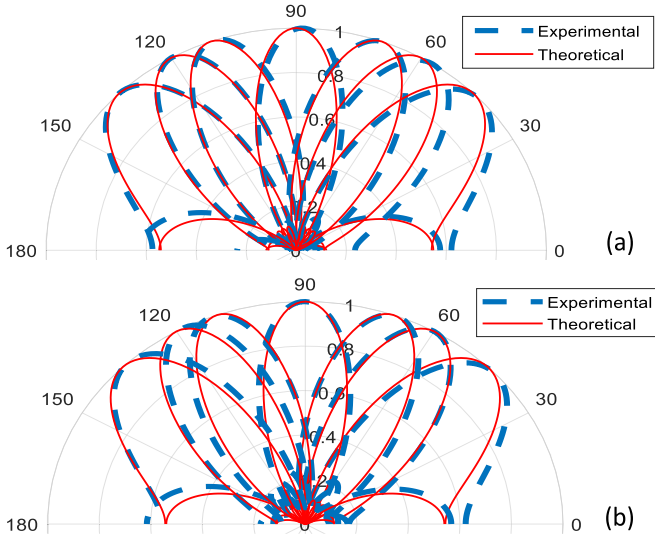

Fig. 10. Theoretical and experimental average array factors after configuring the OBFN PIC to operate with sine waves with central frequencies at (a) 5 GHz and (b) 10 GHz. Target beam angles were 45°, 60°, 70°, 90°, 110°, 120°, and 135°.

modulation format, the symbol rate, the carrier frequency, the type of the pulse shaping filter and the selected roll-off factor for the generation of the microwave signals, as well as the set of the intended beam angles. In all cases, the adjustment of the relative total group time delay that is imposed by the MRRs of each OTTDL is based on eq. (1).

The initial adjustment of the group time delays in each OTTDL was realized utilizing pure sinusoidal waves at either 5 or 10 GHz, depending on the experimental case. Fig. 10 depicts the time average array factors based on the samples acquired from the oscilloscope, when the OBFN-PIC is configured to operate with sinusoidal waves at 5 and 10 GHz, as well as the corresponding theoretical values for all intended beam angles. Despite some slight angle deviation, which is mainly due to the impact of the noise power, the experimental and the theoretical array factors are in good agreement.

In addition to these initial tests, we validate the inherent capability of the OBFN to improve the SNIR at a desired direction, utilizing modulated microwave signals. In order to do that, the OBFN-PIC was configured to steer a 500 Mbaud QPSK signal at 10 GHz to 60° beam angle. Fig. 11(a) shows the array factor as calculated using the samples acquired from the oscilloscope. As observed, the main lobe of the beam is
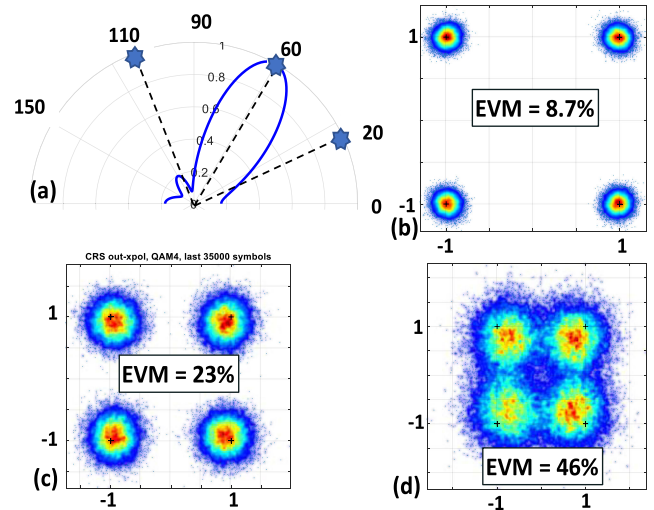
directed to the intended direction, validating that the imposed delays by the three OTTDLs of the OBFN were chosen correctly. Fig. 11(b)–(d) present the reconstructed constellation diagrams at 60°, 20° and 110°. The constellation diagram at 60° is clear and indicates an error-free performance, whereas the constellation diagrams at 20° and 110° are both noisy due to the low signal power propagating to the corresponding directions.

Fig. 12 presents the constellation diagrams for all the experimental cases and every steering beam angle. In each diagram, the calculated EVM values based on the symbols that have been processed are shown as insets. More specifically, in case 1, the EVM ranges from 4.7% up to 6.4% measured at 70° and 110° nominal beam angles, respectively. Similarly, in case 2 the lowest EVM is 7.1% at 90° and the highest 7.8% at 70°, while in case 3 the lowest is 7.6% at 90° and the highest 8.7% at 135°. Thanks to the ultra-low propagation loss of the TriPleX platform (0.1 dB/cm), the elongation of the optical paths via the tuning of the MRRs does not practically affect the power of the signals after the photodetection stage. Therefore, for a given operating microwave frequency, the OBFN can be successfully configured to any arbitrary beam angle without deteriorating the overall transmission performance. Within the system experiments, the maximum delay was 141.4 ps, imposed at the PM1-PD1 link, and corresponds to the case 1 for beam angle at 135°. At these delay settings, the link gain of the PM1-PD1 link at 5 GHz was -38.53 dB, reduced by 0.25 dB compared to the corresponding value of the link gain curve, shown in Fig. 6. Furthermore, the NF at the same frequency was 38.53 dB while the $SFDR_3$ was 89.7 dB·Hz$^{2/3}$.

Since our microwave photonics system is limited by the thermal noise and the operating temperature is stable with an accuracy of 0.0012°C, the observed EVM fluctuation is due to the noise power density of the oscilloscope. In order to minimize this fluctuation and taking into account that the noise power is dictated by the measuring bandwidth, in all the experimental cases the analog bandwidth of the oscilloscope was limited at
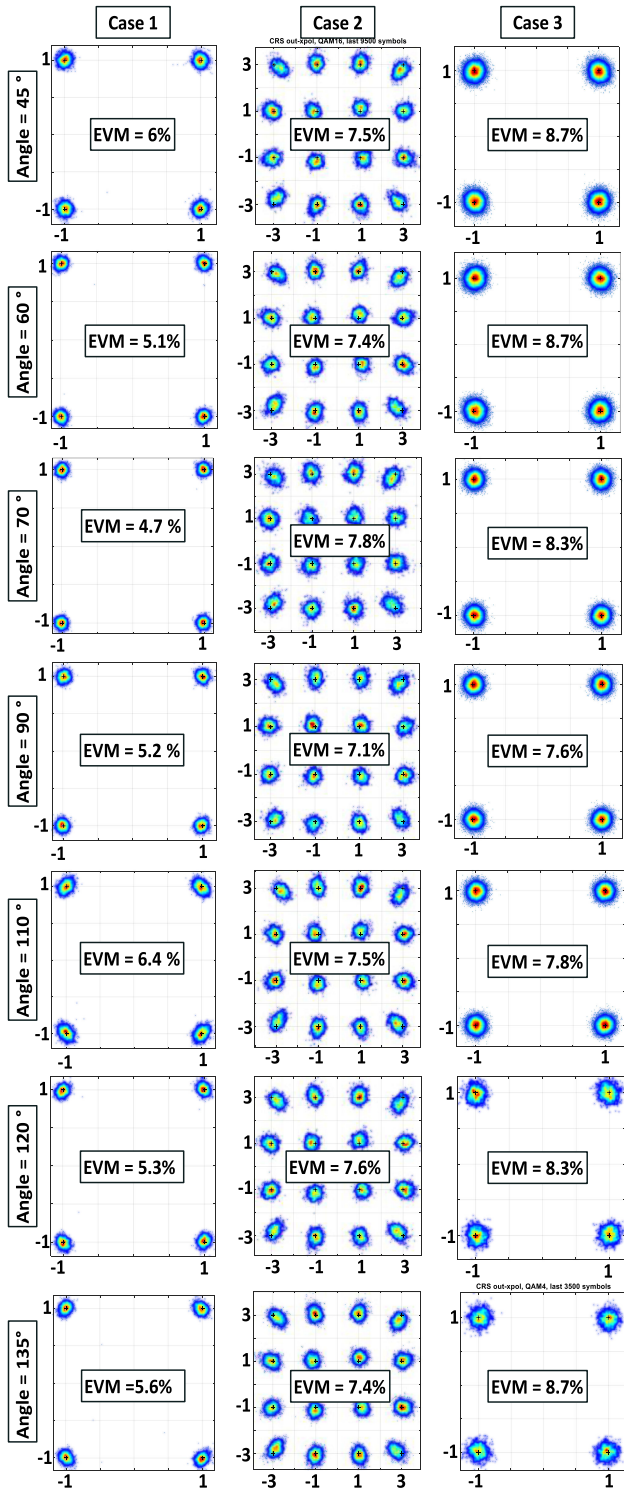
Fig. 12   Reconstructed constellation diagrams for each experimental case. As insets are shown the calculated EVM values.

12 GHz. Finally, it should be noted that the increase of the EVM from the case 1 to the case 3 is due to the fact that the OBFN-PIC has higher NF in the frequency region around 10 GHz compared to the region around 5 GHz, and consequently a lower SNR is achieved in case 3. In all cases, no errors were detected and as a result the calculated BER for cases 1 and 3 is equal to $5 \cdot 10^{-6}$

and $2.5 \cdot 10^{-6}$ for case 2, validating the beamforming potential of the demonstrated OBFN-PIC.

The average power consumption of the OBFN-PIC in these experimental cases was 17.5 W. The sources of the power consumption are the external cavity laser and the thermal phase shifters, which require almost 300 mW each for π phase shift.

IV. CONCLUSION AND OUTLOOK

We have reported on the design, fabrication, and system demonstration of a 1×4 OBFN-PIC based on the hybrid integration of InP components in a TriPleX platform. The prototype is a fully integrated and flexible optical signal processor in a very compact form that can handle and process high-frequency microwave signals purely in the optical domain. Compared to other state-of-the-art integrated optical beamformers, the reported OBFN-PIC stands out due to the co-integration of InP components that can support the generation, modulation, and detection of optical signals on-chip with a TriPleX processing unit that can induce continuously tunable true time delay into four optical paths. More specifically, the OBFN-PIC comprises a hybrid external cavity laser, two InP phase modulators, a TriPleX SSBFC optical filter, four TriPleX OTTDLs based on tunable MRRs, and four InP photodetectors. Thanks to the integration of the high-bandwidth modulators and photodiodes as well as of the eight cascaded MRRs in each OTTDL, the OBFN-PIC can process microwave signals with central frequencies up to 40 GHz and impose continuously tunable time delays over wide operating bandwidths without deteriorating the system performance. To the best of our knowledge, we provided for the first-time a concrete analysis of the system performance of a fully integrated OBFN-PIC. In specific, we have experimentally evaluated the performance of the OBFN-PIC to process microwave signals, by measuring the link gain for operating frequencies from 0.04 GHz up to 40 GHz, and the NF as well as the $SFDR_{2,3}$ at 5 and 10 GHz. The maximum link gain was -36.98 dB measured at 2.6 GHz. The NF was calculated to be equal to 38.28 dB and 41.95 dB at 5 GHz and 10 GHz, respectively, and the $SFDR_2$ and $SFDR_3$ around 5 GHz were 70.5 dB·Hz$^{1/2}$ and 89.9 dB·Hz$^{2/3}$, respectively, whereas around 10 GHz were 67.7 dB·Hz$^{1/2}$ and 88.8 dB·Hz$^{2/3}$, respectively. Furthermore, using 500 Mbaud QAM signals at 5 and 10 GHz as input signals and an experimental setup that emulates the operation of the OBFN-PIC in the downlink direction of a wireless system, we have evaluated the EVM and BER performance of the decoded signals for beam angles ranging from 45° to 135°. In all cases, error-free performance has been successfully achieved. The average power consumption has been equal to 17.5 W. Further improvement in the system performance can be achieved by reducing the coupling loss between the TriPleX and InP platforms to less than 1 dB and by utilizing novel waveguide-based external cavity lasers with a dual gain section that can exhibit on-chip optical powers up to 20.7 dBm [38].

As already described in the previous paragraphs, the demonstrated OBFN architecture can feed a 4-element antenna array and support the formation and steering of a single microwave beam. The OBFN-PIC can be used within the context of mobile

cellular networks to provide high-speed communication to a group of users or a mobile node [44] as well as within satellite networks to underpin for example an aircraft to satellite communication link [45]. Larger antenna arrays may also be supported considering the proposed OBFN-PIC as the key building block of a modular beamforming architecture [45]. Based on a tree topology and several beamforming stages, multiple OBFNs of low size can be connected in series, combined with RF beamforming networks, and feed up to thousands of AEs [45]. However, it is evident that within these architectures, the number of the required thermo-optic phase shifters is increased dramatically and so is the total power consumption that poses a seemingly insurmountable obstacle. In order to alleviate this strict requirement, LioniX Int. has developed a novel type of phase shifters based on the heterogeneous integration of PZTs on the TriPleX platform that requires only 4 mW power consumption for π phase shift and could potentially exhibit reconfiguration times at the μs scale [46]. Using this value, the replacement of all thermal-phase shifters by their PZT-based counterpart in our OBFN-PIC can lead to a total power consumption of less than 0.5 W.

As part of the European project ICT-TERAWAY [47], we are working towards the development of OBFNs based on the hybrid integration of the TriPleX and InP platform using PZT-based phase shifters for application in beyond 5G networks operating in W (92-114.5 GHz), D (130-174.8 GHz) or THz (252-322) bands.

REFERENCES

[1] R. Mailloux, *Phased Array Antenna Handbook*. Norwood, MA, USA: Artech House, 2005.

[2] H. Daniel, Y. Monnai, D. Abbott, C. Fumeaux, and W. Withayachumnankul, "Tutorial: Terahertz beamforming, from concepts to realizations," *APL Photon.*, vol. 3, no. 5, 2018, Art. no. 051101.

[3] J. Capmany and D. Novak, "Microwave photonics combines two worlds," *Nat. Photon.*, vol. 1, no. 6, pp. 319–330, 2007.

[4] J. Yao, "Microwave photonics," *J. Lightw. Technol.*, vol. 27, no. 3, pp. 314–335, 2009, doi: 10.1109/JLT.2008.2009551.

[5] B. Jung, D. Kim, I. Jeon, S. Shin, and H. Kim, "Optical true time-delay beamformer based on microwave photonics for phased array radar," in *Proc. 3rd Int. Asia-Pacific Conf. Synthetic Aperture Radar*, Seoul, Korea (South), 2011, pp. 1–4.

[6] B. Jung, J. Shin, and B. Kim, "Optical true time-delay for two-dimensional X-Band phased array antennas," *IEEE Photon. Technol. Lett.*, vol. 19, no. 12, pp. 877–879, Jun. 2007, doi: 10.1109/LPT.2007.897530.

[7] S. Garcia and I. Gasulla, "Design of heterogeneous multicore fibers as sampled true-time delay lines," *Opt. Lett.*, vol. 40, pp. 621–624, 2015.

[8] S. García, M. Ureña, and I. Gasulla, "Heterogeneous multicore fiber for optical beamforming," in *Proc. Int. Topical Meet. Microw. Photon. (MWP)*, Ottawa, ON, Canada, 2019, pp. 1–4, doi: 10.1109/MWP.2019.8892123.

[9] L. Zhang *et al.*, "Photonic true time delay beamforming technique with ultra-fast beam scanning," *Opt. Exp.*, vol. 25, pp. 14524–14532, 2017.

[10] P. Wu, S. Tang, and D. E. Raible, "A prototype high-speed optically-steered X-band phased array antenna," *Opt. Exp.*, vol. 21, pp. 32599–32604, 2013.

[11] H. Zmuda, R. A. Soref, P. Payson, S. Johns, and E. N. Toughlian, "Photonic beamformer for phased array antennas using a fiber grating prism," *IEEE Photon. Technol. Lett.*, vol. 9, no. 2, pp. 241–243, Feb. 1997, doi: 10.1109/68.553105.

[12] J. Zhang and J. Yao, "Photonic true-time delay beamforming using a switch-controlled wavelength-dependent recirculating loop," *J. Lightw. Technol.*, vol. 34, no. 16, pp. 3923–3929, Aug. 2016, doi: 10.1109/JLT.2016.2583918.

[13] R. Bonjour, S. Welschen, J. F. Johansson, and J. Leuthold, "Steering and shaping of multiple beams with a spatial light modulator based beamformer," in *Proc. Int. Topical Meet. Microw. Photon.*, Toulouse, France, 2018, pp. 1–4, doi: 10.1109/MWP.2018.8552916.

[14] B. Vidal, T. Mengual, C. Ibanez-Lopez, and J. Marti, "Optical beamforming network based on fiber-optical delay lines and spatial light modulators for large antenna arrays," *IEEE Photon. Technol. Lett.*, vol. 18, no. 24, pp. 2590–2592, Dec. 2006, doi: 10.1109/LPT.2006.887347.

[15] C. Tsokos, E. Mylonas, P. Groumas, L. Gounaridis, H. Avramopoulos, and C. Kouloumentas, "Optical beamforming network for multi-beam operation with continuous angle selection," *IEEE Photon. Technol. Lett.*, vol. 31, no. 2, pp. 177–180, Jan. 2019, doi: 10.1109/LPT.2018.2889411.

[16] C. Tsokos *et al.*, "Optical beamforming networks supporting multibeam and multicast operation," in *Proc. 22nd Int. Conf. Transparent Opt. Netw.*, Bari, Italy, 2020, pp. 1–5, doi: 10.1109/ICTON51198.2020.9203380.

[17] J. Wang *et al.*, "Continuous angle steering of an optically- controlled phased array antenna based on differential true time delay constituted by micro-optical components," *Opt. Exp.*, vol. 23, pp. 9432–9439, 2015.

[18] N. Hamdash, A. Sharaiha, T. Rampone, C. Quendo, N. Martin, and D. Le Berre, "Optically controlled RF phase shifts in SOAs by adding the XGM response of an optical signal," *IEEE Photon. Technol. Lett.*, vol. 31, no. 13, pp. 1060–1063, Jul. 2019, doi: 10.1109/LPT.2019.2918074.

[19] P. Berger, J. Bourderionnet, F. Bretenaker, D. Dolfi, and M. Alouini, "Time delay generation at high frequency using SOA based slow and fast light," *Opt. Exp.*, vol. 19, pp. 21180–21188, 2011.

[20] R. Bonjour, S. A. Gebrewold, D. Hillerkuss, C. Hafner, and J. Leuthold, "Ultra-fast tunable true-time delay using complementary phase-shifted spectra (CPSS)," in *Proc. Opt. Fiber Commun. Conf. Exhib.*, Los Angeles, CA, USA, 2015, pp. 1–3, doi: 10.1364/OFC.2015.W2A.67.

[21] C. Tsokos *et al.*, "Analysis of a multibeam optical beamforming network based on blass matrix architecture," *J. Lightw. Technol.*, vol. 36, no. 16, pp. 3354–3372, Aug. 2018, doi: 10.1109/JLT.2018.2841861.

[22] C. J. Chung, X. Xu, G. Wang, Z. Pan, and R. T. Chen, "On-chip optical true time delay lines featuring one-dimensional fishbone photonic crystal waveguide," *Appl. Phys. Lett.*, vol. 112, no. 7, 2018, Art. no. 071104.

[23] J. Sancho *et al.*, "Integrable microwave filter based on a photonic crystal delay line," *Nature Commun.*, vol. 3, 2012, Art. no. 1075. [Online]. Available: https://doi.org/10.1038/ncomms2092

[24] J. Wang *et al.*, "Subwavelength grating enabled on-chip ultra-compact optical true time delay line," *Sci. Rep.*, vol. 6, 2016, Art. no. 30235. [Online]. Available: https://doi.org/10.1038/srep30235

[25] J. Xie, L. Zhou, Z. Li, J. Wang, and J. Chen, "Seven-bit reconfigurable optical true time delay line based on silicon integration," *Opt. Exp.*, vol. 22, pp. 22707–22715, 2014.

[26] C. Zhu *et al.*, "Silicon integrated microwave photonic beamformer," *Optica*, vol. 7, pp. 1162–1170, 2020.

[27] P. Zheng *et al.*, "A wideband 1×4 optical beam-forming chip based on switchable optical delay lines for Ka-band phased array," *Opt. Commun.*, vol. 488, no. 126842, 2021.

[28] R. L. Moreira *et al.*, "Integrated ultra-low-loss 4-bit tunable delay for broadband phased array antenna applications," *IEEE Photon. Technol. Lett.*, vol. 25, no. 12, pp. 1165–1168, Jun. 2013, doi: 10.1109/LPT.2013.2261807.

[29] Q. Cheng, S. Zheng, Q. Zhang, J. Ji, H. Yu, and X. Zhang, "An integrated optical beamforming network for two-dimensional phased array radar," *Opt. Commun.*, vol. 489, 2021, Art. no. 126809.

[30] V. Duarte *et al.*, "Modular coherent photonic-aided payload receiver for communications satellites," *Nature Commun.*, vol. 10, no. 1, pp. 1–9, 2019.

[31] L. Zhuang, C. G. H. Roeloffzen, R. G. Heideman, A. Borreman, A. Meijerink, and W. van Etten, "Single-chip ring resonator-based 1x8 optical beam forming network in CMOS-compatible waveguide technology," *IEEE Photon. Technol. Lett.*, vol. 19, no. 15, pp. 1130–1132, Aug. 2007, doi: 10.1109/LPT.2007.900313.

[32] Y. Liu *et al.*, "Ultra-low-loss silicon nitride optical beamforming network for wideband wireless applications," *IEEE J. Sel. Topics Quantum Electron.*, vol. 24, no. 4, Jul./Aug. 2018, Art. no. 8300410, doi: 10.1109/JSTQE.2018.2827786.

[33] M. Burla *et al.*, "Multiwavelength-integrated optical beamformer based on wavelength division multiplexing for 2-D phased array antennas," *J. Lightw. Technol.*, vol. 32, no. 20, pp. 3509–3520, Oct. 2014, doi: 10.1109/JLT.2014.2332426.

[34] N. M. Tessema *et al.*, "A tunable Si3N4 integrated true time delay circuit for optically-controlled K-Band radio beamformer in satellite communication," *J. Lightw. Technol.*, vol. 34, no. 20, pp. 4736–4743, Oct. 2016, doi: 10.1109/JLT.2016.2585299.

[35] A. Leinse *et al.*, "Hybrid interconnection of InP and TriPleX photonic integrated circuits for new module functionality," *Opt. Interconnects XIX*, vol. 10924. International Society for Optics and Photonics, 2019.

[36] I. Visscher *et al.*, "Broadband true time delay microwave photonic beamformer for phased array antennas," in *Proc. 13th Eur. Conf. Antennas Propag. (EuCAP)*, Krakow, Poland, 2019, pp. 1–5.

[37] R. Grootjans *et al.*, "Broadband continuously tuneable delay microwave photonic beamformer for phased array antennas," in *Proc. 14th Eur. Microw. Integr. Circuits Conf. (EuMIC)*, Paris, France, 2019, pp. 258–261, doi: 10.23919/EuMIC.2019.8909572.

[38] J. P. Epping *et al.*, "Hybrid integrated silicon nitride lasers," in *Proc. Phys. Simul. Optoelectron. Devices XXVIII*, vol. 11274, International Society for Optics and Photonics, 2020, Art. no. 112741L.

[39] V. J. Urick, K. J. Williams, and J. D. McKinney, *Fundamentals of Microwave Photonics*. Hoboken, NJ, USA: Wiley, 2015.

[40] Y. Shi, L. Yan, and A. E. Willner, "High-speed electrooptic modulator characterization using optical spectrum analysis," *J. Lightw. Technol.*, vol. 21, no. 10, pp. 2358–2367, Oct. 2003, doi: 10.1109/JLT.2003.818162.

[41] S. G. Hailu and S. L. Lee, "Tunable optical delay line based on a racetrack resonator with tunable coupling and stable wavelength," *Appl. Sci.*, vol. 9, no. 24, 2019, Art. no. 5483.

[42] C. Kouloumentas *et al.*, "Multi-rate and multi-channel optical equalizer based on photonic integration," *IEEE Photon. Technol. Lett.*, vol. 32, no. 23, pp. 1465–1468, Dec. 2020, doi: 10.1109/LPT.2020.3035506.

[43] L. Zhuang, M. Hoekman, R. M. Oldenbeuving, K. Boller, and C. G. H. Roeloffzen, "CRIT-Alternative narrow-passband waveguide filter for microwave photonic signal processors," *IEEE Photon. Technol. Lett.*, vol. 26, no. 10, pp. 1034–1037, May 2014, doi: 10.1109/LPT.2014.2312718.

[44] P. Groumas *et al.*, "Photonic integration technology for the interface between the optical and wireless part in 5G networks: The H2020-ICT-HAMLET approach," in *Proc. IEEE Photon. Soc. Summer Topical Meet. Ser.*, 2017, pp. 57–58, doi: 10.1109/PHOSST.2017.8012649.

[45] L. Bliek *et al.*, "Automatic delay tuning of a novel ring resonator-based photonic beamformer for a transmit phased array antenna," *J. Lightw. Technol.*, vol. 37, no. 19, pp. 4976–4984, Oct. 2019, doi: 10.1109/JLT.2019.2926621.

[46] J. P. Epping *et al.*, "Ultra-low-power stress-based integrated photonic phase actuator," in *Proc. Eur. Conf. Integr. Opt.*, Valencia, Spain, 2018. [Online]. Available: https://www.ecio-conference.org/2018-proceedings/session-programmable-and-reconfigurable-pics/

[47] 5G-PPP Annual Journal 2021, pp. 69–71, 2021. [Online]. Available: https://ict-teraway.eu/wp-content/uploads/2021/05/5G-European-Annual-Journal-2021.pdf